Research Article

Nano Research
2023, 16(4): 5834–5842

ISSN 1998-0124 CN 11-5974/O4
https://doi.org/10.1007/s12274-022-5213-6

Designing two-dimensional ferroelectric materials from phosphorus-analogue structures

Ziyuan Liu[1,2], Lei Tao[2], Yan-Fang Zhang[2], Jinbo Pan[1,3] (✉), and Shixuan Du[1,2,3,4] (✉)

[1] *Beijing National Laboratory for Condensed Matter Physics, Institute of Physics, Chinese Academy of Sciences, Beijing 100190, China*
[2] *University of Chinese Academy of Sciences, Chinese Academy of Sciences, Beijing 100190, China*
[3] *Songshan Lake Materials Laboratory, Dongguan 523808, China*
[4] *CAS Center for Excellence in Topological Quantum Computation, Beijing 100190, China*

Received: 13 September 2022 / **Revised:** 15 October 2022 / **Accepted:** 15 October 2022

ABSTRACT

Two-dimensional (2D) ferroelectric (FE) materials with relatively low switching barrier and large polarization are promising candidates for next-generation miniaturized nonvolatile memory devices. Herein, we screen out 39 new 2D ferroelectric materials, MX (M: Group III-V elements; X: Group V-VII elements), in three phosphorus-analogue phases including black phosphorene-like α-phase, blue phosphorus-like β-phase, and GeSe-like γ-phase using high-throughput calculations. Seven materials (α-SbP, γ-AsP, etc.) exhibit FE switching barriers lower than 0.3 eV/f.u., ferroelectric polarization larger than 2×10^{-10} C/m, and high thermodynamic stability with energy above hull smaller than 0.2 eV/atom. We find that the larger the electronegativity difference between M and X, the larger the ferroelectric polarization. Moreover, larger electronegativity differences result in lower in-plane piezoelectric stress tensor (e_{11}) for MX consisting of Group IV and VI elements and larger e_{11} for those consisting of Group V elements. Further calculations predict a giant tunneling electroresistance in ferroelectric tunnel junction α-Sb(Sn)P/α-SbP/α-Sb(Te)P (1.26×10^4%) and large piezoelectric strain coefficient in α-SnTe (396 pm/V), providing great opportunities to the design of non-volatile resistive memories, and high-performance piezoelectric devices.

KEYWORDS

two-dimensional (2D) materials, ferroelectricity, piezoelectricity, ferroelectric tunnel junction

1 Introduction

Ferroelectric (FE) materials, displaying spontaneous electric polarization that can be switched by an electric field, with relatively low switching barrier and large polarization, have great potential applications in nonvolatile memory devices, sensors, field effect transistors (FET) and solar cells [1, 2]. The recent discoveries of two-dimensional (2D) ferroelectric materials have gained considerable attention due to appealing physical properties, such as ultra-thin thickness [3, 4], dangling bond-free surfaces/interfaces [5], and the feasibility of non-volatile manipulation of other exotic properties [6–8].

Substantial efforts have been devoted to searching 2D ferroelectric materials in recent years [9–12], but a small number of 2D ferroelectric materials have been experimentally synthesized, such as In_2Se_3 [4, 13], $CuInP_2S_6$ [3], distorted 1T (d1T)-$MoTe_2$ [14], and SnX (X = S, Se, Te) [15–17]. Among them, the binary compounds with the MX (M: Metal, X: Anion) stoichiometry have gained particular interest. The MX compounds with 10 valence electrons are supposed to be phosphorus-analogues. Due to the different arrangement of lone pairs [18], multiple monolayer phases are possibly created [19]. Among these MX compounds, the α-phase with black phosphorene-like puckered structure [20], the β-phase with blue phosphorus-like buckled structure [21], and the γ-phase with GeSe-like boat conformation structure [22, 23], possess both generally low formation enthalpies and non-centrosymmetric structures, whereby driving the system into a polarized state. In addition, Zeng, et al. [20] and Qian, et al. [24] successively reported the multiferroicity in the α-phase of Group IV monochalcogenides.

The unique combination of ferroelasticity and ferroelectricity in these 2D multiferroics allows switching of lattice orientation and electrical polarization simultaneously. Later, Qian, et al. also found a nonlinear optical properties in these multiferroic materials, active electrical/optical/mechanical switching of ferroic orders in 2D multiferroics, and *in situ* ultrafast optical characterization of local atomistic and electronic structures using noncontact noninvasive optical second harmonic generation (SHG) techniques can be achieved [25].

As demonstrated by previous literature, the systems with isoelectronic nature tend to harbor similar electronic properties [26]. Fundamental questions arising are whether we can design new 2D MX FE materials with even better performance, and what the intrinsic physic mechanism is for different properties of these materials with similar geometric structures but different chemical compositions.

In this work, we screen out 2D MX FE materials made up of Group III-VII elements with 10 valence electrons by "atomic transmutation" [27] based on high-throughput calculations. Three possible phases, including α-phase, β-phase, and γ-phase, are considered. We identify 55 2D ferroelectric MX materials

Address correspondence to Jinbo Pan, jbpan@iphy.ac.cn; Shixuan Du, sxdu@iphy.ac.cn

including 39 new compounds out of 150 combinations. The high throughput results enable the extraction of periodic trends and fundamental rules related to ferroelectric properties of 2D MX compounds, revealing a vitally important role in the synergistic effect between dynamical charge transfer, and the main factor influenced by electronegativity and structural distortion. For the same M atom (cation), the greater electronegativity difference between M and X, the more charge transfer, and the larger ferroelectric polarization for most of the MX compounds. In addition, the in-plane piezoelectricity calculations also demonstrate a close correlation between the electronegativity difference and structural distortion. Furthermore, a giant tunneling electroresistance (TER) effect of 1.26×10^4%, far beyond the reported in-plane ferroelectric tunnel junction (FTJ), is achieved in α-Sb(Sn)P/α-SbP/α-Sb(Te)P FTJ. Besides, α-SnTe is found to own giant piezoelectric strain coefficient (d_{11}, 396 pm/V), which is larger than the reported in-plane ones.

2 Results and discussion

Our design rule for the identification of new 2D ferroelectric materials is "atomic transmutation", in which transmuting one type of element into its neighboring elements in the periodic table while preserving the same number of valence electrons. The three different non-centrosymmetric structural phases with the same MX stoichiometry we considered are shown in Fig. 1(a). Both α-phase and γ-phase materials contain two cation atoms and two anion atoms per primitive cell with a $Pmn2_1$ space group, while β-phase materials contain only one cation atom and one anion atom with a P3m1 space group. To guarantee 10 valence electrons, MX compounds can be made up of Group III and VII elements, Group IV and VI elements, or only Group V elements, where M is cation in the grey shaded region and X is anion in the pink shaded region as shown in Fig. 1(b).

Our screening process for 2D ferroelectric materials is shown in Fig. 1(c). First, 150 possible MX structures are constructed within all the combinations preserving the 10 valence electrons in three phases. After structural optimization, 81 candidates maintain their initial non-centrosymmetric structures and are selected for the next screening step. We then evaluate their dynamical stabilities via phonon spectra analysis and find 55 stable structures without imaginary frequencies. Notably, there are 39 new MX compounds despite of the 16 previously known MX compounds. Their electronic bandgaps are summarized in Table 1, and their phonon spectra are shown in Fig. S1 in the Electronic Supplementary Material (ESM). We take α-SbAs as an example to compare the band structure with and without considering spin-orbit coupling (SOC) effect as shown in Figs. S2(a) and S2(b) in the ESM, respectively. The band shape and bandgap with and without SOC effect are similar (bandgap difference is around 0.02 eV), so we neglect the SOC effect on electronic properties for all structures in this work.

The formation enthalpies of MX compounds are used to calculate the energy above convex hull (E_{hull}) [28, 29], which is of vital importance for experimental synthesis, however, often be neglected. Here, $\Delta H = (E_{MX} - E_M - E_X)/2$, where E_{MX} is the total energy of MX monolayer, and E_M and E_X are the chemical potentials of M and X elements under their ground states, respectively. The thermodynamic stability of a compound is evaluated in terms of its E_{hull}, which gives the energy of the material relative to other competing phases of the same chemical composition, including mixed phases [30, 31]. As listed in Table 1, around one-third of the 55 materials have negative formation enthalpy ($\Delta H < 0$) and 32 materials show E_{hull} smaller than 0.2 eV/atom, indicating high thermodynamic stabilities of these materials. Till now, only 2D ferroelectric SnS, SnSe, and SnTe have been synthesized, and we expect experimental constructions of novel 2D MX ferroelectric materials based on our prediction.

The origin of the ferroelectric properties of these 55 materials is centrosymmetry breaking induced spontaneous polarization. Here, we define the vertical distance between M atom and X atom, which causes structural distortion as d. We define d along the x-direction as d_x and that along the z-direction as d_z, as shown in Fig. 2(a). For these ferroelectric materials, two stable phases related to a spatial inversion are denoted as A phase with a positive polarization value (P_s) and A' phase with the same polarization value in the opposite direction ($-P_s$). A centrosymmetric structure without spontaneous polarization is defined as B phase ($d = 0$). Taking α-BiSb, β-TlI, and γ-SiTe in B phase as the representative examples of these three phases, their phonon spectra show imaginary frequencies as shown in Fig. 2(b). These imaginary frequencies indicate that they are all dynamically unstable. The soft optical phonon modes at a, b, and c points in Fig. 2(b) correspond to the movements of neighboring M and X atoms towards opposite directions, leading to the formation of ferroelectric phases. More specifically, d_x causes the in-plane polarization for α-phase and γ-phase, while d_z causes the out-of-plane polarization for β-phase.

The energy difference between A phase and B phase is the

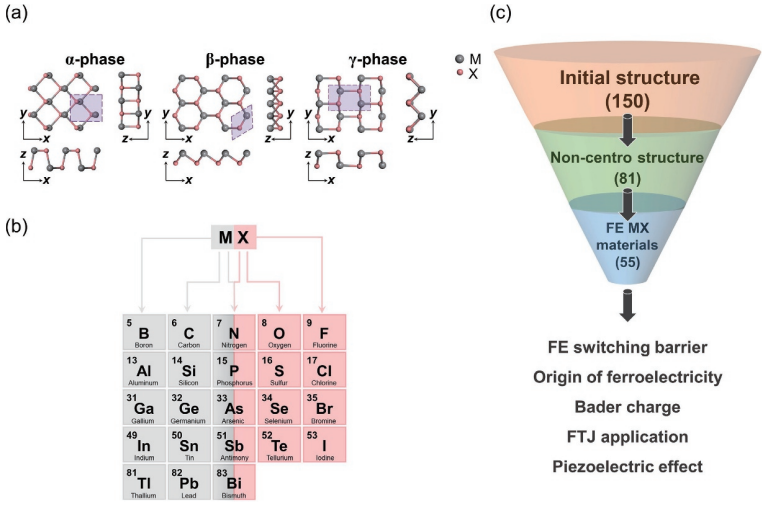

Figure 1 Atomic configurations, compounds, and screening workflow of three phases 2D ferroelectric MX materials. (a) Top and side views of geometric structures of α-phase, β-phase, and γ-phase crystals. The purple regions mark the primitive cells. Grey and pink balls denote cation and anion atoms, respectively. (b) The binary MX systems composed of an M atom in grey shaded area and an X atom in pink shaded area. (c) Screening workflow for 2D ferroelectric MX materials.

Table 1 Bandgap, formation enthalpies (ΔH), energy above convex hull (E_{hull}), ferroelectric switching barrier (E_b), and vertical distance between M atom and X atom which causes structural distortion (d) and spontaneous polarization (P_s) of 55 selected ferroelectrics

Phase	Material	Bandgap (eV)	ΔH (eV)	E_{hull} (eV)	E_b (eV/f.u.)	d (Å)	P_s (10^{-10} C/m)	
							This work	Previous literatures
α-phase	SiS	1.430	−0.374	0.465	0.672	0.862	6.388	
	SiSe	1.209	0.071	0.409	0.410	0.693	5.757	
	SiTe	0.394	0.259	0.259	0.043	0.306	4.167	4.200 [69]
	GeS	1.775	−0.503	0.082	0.280	0.624	5.017	4.840 [24]
	GeSe	1.160	−0.144	0.065	0.061	0.375	3.613	3.570 [24]
	GeTe	0.869	0.016	0.111	0.023	0.276	3.161	3.280 [69]
	SnS	1.482	−0.734	0.044	0.027	0.350	2.803	2.600 [24]
	SnSe	0.937	−0.393	0.045	0.007	0.232	2.035	1.810 [24]
	SnTe	0.711	−0.226	0.069	0.0004	0.100	1.033	1.940 [69]
	PbO	2.474	−1.427	0.050	0.045	0.419	3.248	2.410 [70]
	AsN	1.900	0.173	0.173	1.601	0.979	5.286	
	AsP	0.902	0.097	0.097	0.752	0.742	4.327	
	SbN	1.779	0.217	0.217	0.937	0.853	6.380	7.810 [71]
	SbP	0.507	0.154	0.154	0.264	0.501	4.818	
	SbAs	0.223	0.072	0.087	0.226	0.489	3.467	
	BiN	1.458	0.429	0.429	0.155	0.477	5.793	5.800 [72]
	BiP	0.570	0.197	0.197	0.143	0.427	4.951	5.350 [71]
	BiAs	0.527	0.081	0.081	0.134	0.408	2.791	
	BiSb	0.459	0.108	0.116	0.093	0.369	2.392	
β-phase	BI	1.784	1.669	1.711	0.359	1.430	0.111	
	InF	1.871	−1.751	0.153	0.216	1.131	0.138	
	TlI	2.615	−0.504	0.177	0.021	1.615	0.194	
	TeC	1.283	1.750	1.750	0.600	1.115	0.232	
	SiS	2.195	−0.383	0.456	0.602	1.326	0.012	
	SiSe	2.126	0.054	0.393	1.118	1.418	0.021	
	SiTe	1.828	0.288	0.288	1.006	1.529	0.034	
	GeO	2.108	−1.187	0.380	0.886	0.989	0.263	
	GeS	2.487	−0.482	0.103	1.025	1.357	0.082	
	GeSe	2.283	−0.130	0.079	0.916	1.446	0.071	0.065 [73]
	GeTe	1.781	0.048	0.143	0.693	1.561	0.030	
	SnS	2.322	−0.658	0.120	0.585	1.459	0.122	
	SnTe	1.888	−0.168	0.127	0.672	1.690	0.065	
	PbO	1.744	−1.138	0.339	0.242	0.923	0.253	
	PbS	2.026	−0.618	0.247	0.457	1.438	0.223	
	PbSe	1.854	−0.331	0.230	0.484	1.549	0.189	
	PbTe	1.602	−0.197	0.209	0.567	1.690	0.146	29.2 [21]
	AsN	1.963	0.437	0.437	1.214	0.957	0.200	
	AsP	1.835	0.077	0.077	1.282	1.321	0.049	
	SbN	1.671	0.507	0.507	0.944	1.014	0.107	
	SbP	1.728	0.164	0.164	1.171	1.438	0.087	
	SbAs	1.471	0.054	0.070	0.916	1.517	0.043	
	BiN	0.707	0.771	0.771	0.497	1.047	0.297	
	BiP	1.443	0.263	0.263	0.798	1.482	0.155	
	BiAs	1.059	0.108	0.108	0.892	1.559	0.107	
	BiSb	0.956	0.120	0.128	0.834	1.690	0.059	
γ-phase	SiSe	0.419	0.087	0.426	0.011	0.235	1.964	

(Continued)

Phase	Material	Bandgap (eV)	ΔH (eV)	E_{hull} (eV)	E_b (eV/f.u.)	d (Å)	P_s (10^{-10} C/m)	
							This work	Previous literatures
γ-phase	SiTe	1.088	0.303	0.303	0.005	0.175	1.875	
	GeSe	1.68	−0.121	0.088	0.006	0.224	1.761	1.590 [23]
	AsN	0.238	0.245	0.245	0.315	0.548	4.664	
	AsP	0.139	0.147	0.147	0.140	0.375	4.338	
	SbP	0.83	0.196	0.196	0.072	0.331	3.465	3.470 [22]
	SbAs	0.82	0.103	0.118	0.086	0.349	3.809	3.800 [22]
	BiP	0.253	0.250	0.250	0.043	0.296	2.996	
	BiAs	0.122	0.127	0.127	0.055	0.320	3.299	
	BiSb	0.153	0.153	0.161	0.044	0.291	3.356	

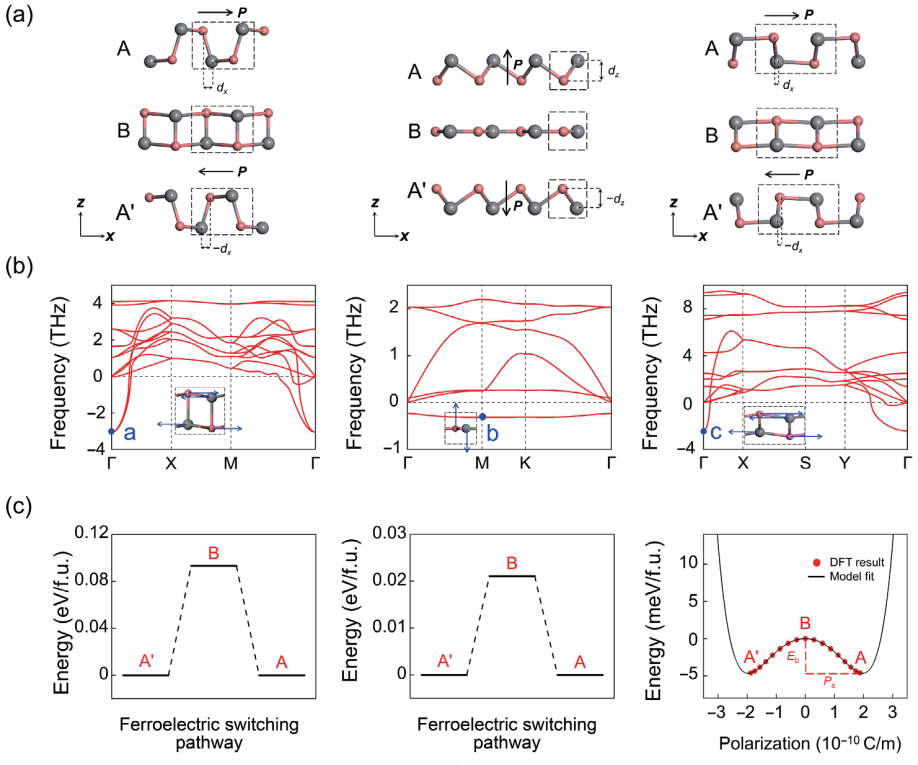

Figure 2 Structures of A phase, B phase, and A' phase, phonon dispersions of B phase, FE switching barrier, and double-well potential vs. polarization of the representative materials in α-phase, β-phase, and γ-phase. (a) Side views of the atomic structures of two distorted phases A and A' and the centrosymmetric B phase in α-phase, β-phase, and γ-phase; the black arrows represent the polarization directions. d_x and d_z indicate the vertical distance between M atom and X atom, which causes structural distortion along the x-direction and z-direction, respectively. (b) Phonon dispersions of centrosymmetric α-BiSb, β-TlI, and γ-SiTe, respectively. Schematics of the largest vibrational modes marked in a, b, and c points. The inset shows that M and X atoms vibrate along the blue arrows. (c) The ferroelectric switching barrier between two ferroelectric phases (A and A') for α-BiSb from the CI-NEB method, β-TlI obtained from the SSNEB method, and double-well potential vs. polarization for γ-SiTe. Red dots are the DFT-calculated total energies and the black curve is the model-fitted energy as a function of polarization.

switching barrier of ferroelectric transition, which can be performed by climbing image nudged elastic band (CI-NEB) calculations for α-phase and γ-phase with in-plane polarization [32, 33], and solid-state nudged elastic band (SSNEB) method [34] for β-phase with out-of-plane polarization because of the required change in the cell size for minimizing the ferroelectric transition barrier, respectively. The lowest transition barriers (E_b) in different phases are 0.093 eV per formula unit (eV/f.u.) for α-BiSb, 0.021 eV/f.u. for β-TlI, and 0.005 eV/f.u. for γ-SiTe, respectively, as shown in Fig. 2(c). The E_b of all the screened MX materials is listed in Table 1. Relatively low E_b indicates that a low electric field will switch the direction of the electric polarization, which is required for ferroelectric devices with low power consumption [23]. There are 26 MX materials listed in Table 1 have relatively low E_b, which is less than 0.3 eV/f.u.

The FE polarization value is another important parameter to evaluate the ferroelectric performance. It defines the change of the sum of the collection of charge multiply atomic positions per unit length [35] along the path of atomic displacement from the high-symmetry phase [36]. A relatively large P_s indicates that the ferroelectric material applied in nonvolatile memory devices will show clearly high and low current states after writing with opposite voltage stripes. We use Berry-phase approach [37, 38] to calculate P_s of these 55 materials. According to the Landau–Ginzburg theory, the total energy of a FE material as a function of spontaneous polarization can be described by the expansion (Eq. (1))

$$E = \sum_i \frac{A}{2}(P_i^2) + \frac{B}{4}(P_i^4) + \frac{C}{6}(P_i^6) + \frac{D}{2}\sum_{<i,j>}(P_i - P_j)^2 \quad (1)$$

where P_i and P_j label the polarization of the i-th and j-th unit cell,

<i,j> denotes the nearest neighbors, and the coefficients *A*, *B*, *C*, and *D* can be fitted by density functional theory (DFT) results. The first three terms are associated with the energy contributed by the polarization in the *i*-th unit cell and the last term is the interaction energy between neighboring *i*-th and *j*-th unit cell. Here, we take γ-SiTe as an example, and the total energy versus P_s of γ-SiTe is plotted in red dots as shown in Fig. 2(c). We use first three terms to fit these red dots and get an anharmonic double-well energy curve, matching well with the Landau–Ginzburg theory. The values of fitting characters *A*, *B*, and *C* for the γ-SiTe monolayers are −7.815, 1.350, and 0.102 (their units are chosen such that the free energy is in units of eV/f.u. if P is in units of 10^{-10} C/m), respectively. The calculated P_s results of the other materials are listed in Table 1. Previously reported P_s results are also listed for comparison, which are consistent with our calculated results. Among them, 25 MX materials have large P_s more than 2×10^{-10} C/m. In particular, 7 materials, including α-SbP, α-SbAs, α-BiAs, α-BiSb, γ-AsP, γ-BiAs, and γ-BiSb, are found to harbor high thermodynamic stabilities (E_{hull} < 0.2 eV/atom), high thermal stabilities (Fig. S3 in the ESM), relatively low FE switching barriers (E_b < 0.3 eV/f.u.), and large polarization magnitudes ($P_s > 2 \times 10^{-10}$ C/m). Considering the SnX (X = S, Se, Te) monolayers [15–17] are experimentally grown by molecular beam epitaxy (MBE) or physical vapor deposition (PVD) on substrates, these 7 most promising materials thus call for experimental realization by using similar approaches.

To explore the possible polarization trend of these materials, we plot the P_s of MX compounds in αn compounds phase with symbols in blue in Fig. 3, while those in γ-phase are shown in Fig. S5(a) in the ESM. Notably, when changing the X and fixing the M, the polarization values of most of materials decrease upon increasing atomic number of X. Since the ferroelectric polarization represents the charge polarization caused by the asymmetry of positive and negative charge centers [35]. The charge transfer between neighboring atoms would definitely influence the ferroelectric property [36]. We thus analyze the dynamical charge transfer between the M and X atoms by calculating the Bader charge [39] marked as red symbols in Fig. 3. The Bader charge results indeed show similar trend with the polarization, verifying a strong but not linear (Fig. S4 in the ESM) correlation between the ferroelectric polarization values and the Bader charge. Taking the α-phase AsX (α-AsN and α-AsP) as a typical example, the polarization values and Bader charge transfer decrease from α-AsN to α-AsP in magnitude with the reduction of the electronegativity difference between As and X atoms. However, β-SiS, β-SiSe, and β-SiTe show reverse trend because of the vertical distance between M atom and X atom, which causes structural distortion and also plays an important role in determining the ferroelectric polarization. Larger *d* results in larger P_s for β-SiS, β-SiSe, and β-SiTe as shown in Fig. S5(c) in the ESM. Spontaneous polarization and vertical distance between M atom and X atom which causes structural distortion of α-phase and γ-phase MX systems, are shown in Figs. S5(b) and S5(d) in the ESM.

2D ferroelectrics can be applied in many potential applications. Here, we take α-SbP with large in-plane ferroelectric polarization (4.82×10^{-10} C/m) as an example to build an in-plane FTJ. In our study, the FTJ consists of three parts: Left electrode, right electrode, and central region. By calculating the band structures of doped α-SbP, one Sb atom was replaced by Sn (Te) atom in a 4 × 1 supercell, as shown in Figs. S2(c) and S2(d) in the ESM. We find that the α-SbP becomes a p-type (n-type) semiconductor. Therefore, we use p-type α-Sb(Sn)P and n-type α-Sb(Te)P as the left and right electrodes of the 2D-FTJ as shown in Fig. 4(a). The central scattering region contains 34 unit cells with a length of about 15 nm. The device configurations for $P_{\rightarrow}$ and $P_{\leftarrow}$ states are explicitly shown in Fig. 4(b).

The tunneling conductance of FTJ can be calculated by the Landauer–Büttiker formula (Eq. (2))

$$G = G_0 \sum_{k_{||}} T(k_{||},E), G_0 = \frac{2e^2}{h} \quad (2)$$

where *e* is the electron charge, *h* is the Planck's constant, G_0 is the conductance quantum, and $T(k_{||},E)$ is the transmission probability at the Fermi energy *E* with Bloch wave vector $k_{||} = (k_x,k_y)$. Here, we focus on the transmission coefficient $T(k_{||},E_F)$ at the Fermi energy

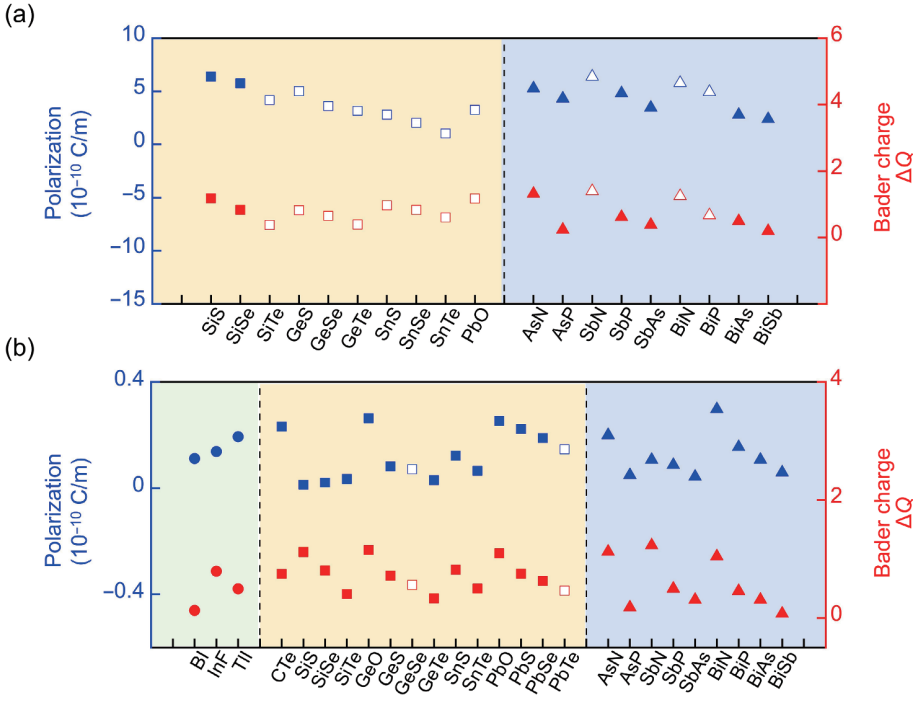

Figure 3 Spontaneous polarization (top blue points) and Bader charge (bottom red points) of (a) α-phase and (b) β-phase MX compounds. Green, yellow, and blue regions represent MX binary compounds consisting of Group III and VII elements (circles), Group IV and VI elements (squares), and Group V elements (triangles), respectively. The hollow symbols represent previously predicted compounds, while the solid symbols represent newly discovered MX in this work.

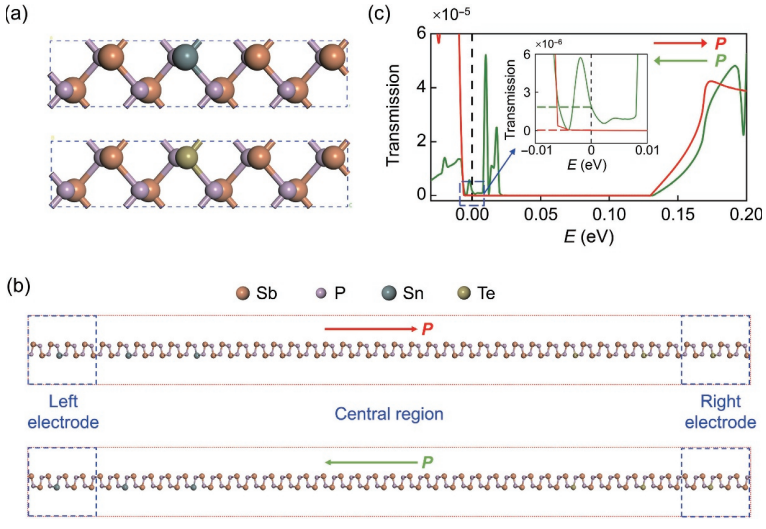

Figure 4 Configurations and transmission of the α-Sb(Sn)P/α-SbP/α-Sb(Te)P FTJ device. (a) Top views of one supercell of the left and right electrodes for $P_{\rightarrow}$ state. Orange, purple, grey, and yellow balls denote Sb, P, Sn, and Te atoms, respectively. (b) Schematics of the FTJ with polarization pointing to right (top) and left (bottom). (c) The transmission through the 2D-FTJ α-Sb(Sn)P/α-SbP/α-Sb(Te)P for $P_{\rightarrow}$ (red lines) and $P_{\leftarrow}$ (green lines) states. The zoom-in shows the transmission from −0.01 to 0.01 eV for $P_{\rightarrow}$ and $P_{\leftarrow}$ state.

that $E = E_F$. To quantify the change in transmission probability between the two opposite ferroelectric polarization directions, the known TER ratio can be defined as Eq. (3) [40]

$$\mathrm{TER} = \frac{|G_{\leftarrow} - G_{\rightarrow}|}{\min(G_{\rightarrow}, G_{\leftarrow})} \times 100\% \quad (3)$$

Here, $G_{\rightarrow}(G_{\leftarrow})$ is the conductance of the FTJ for $P_{\rightarrow}(P_{\leftarrow})$ state. In our result, $G_{\rightarrow} = 1.53 \times 10^{-8}\ G_0$ and $G_{\leftarrow} = 1.94 \times 10^{-6}\ G_0$ as shown in Fig. 4(c). Therefore, we get a giant TER radio TER = 1.26×10^{4}%, which is much larger than predicted in-plane In:SnSe/SnSe/Sb:SnSe FTJ (TER = 1,460%) [41] and in-plane graphene/BiP FTJ (TER = 623%) [42].

In addition, all ferroelectrics represent piezoelectricity due to their non-centrosymmetric structures. Then we explore the piezoelectric properties of these screened ferroelectric MX materials. We calculate the linear piezoelectric stress coefficient $e_{ij} = \frac{\partial P_i}{\partial \varepsilon_j}$ by evaluating the change of polarization P obtained by the Berry-phase method along the i-direction after imposing uniaxial strain ε ranging from −0.5% to 0.5% with steps of 0.1% along the j-direction. Here, we consider the relaxed-ion coefficients that are expected to be experimentally observable with the atomic positions fully relaxed under strain. Besides, we also discuss the piezoelectric strain coefficient $d_{ij} = \frac{\partial P_i}{\partial \sigma_j}$, where σ_j is the stress along the j-direction. The piezoelectric tensors e_{ij} and d_{ij} are defined as Eq. (4)

$$e_{ij} = \frac{dP_i}{d\varepsilon_j} = \frac{\partial P_i}{\partial \sigma_m}\frac{\partial \sigma_m}{\partial \varepsilon_j} = d_{im}C_{mj} \quad (4)$$

Here, C_{mj} is the elastic tensor. For α-phase and γ-phase, the piezoelectric tensors are $d_{11} = \frac{e_{11}C_{22} - e_{12}C_{12}}{C_{11}C_{22} - C_{12}^2}$ and $d_{12} = \frac{e_{12}C_{11} - e_{11}C_{12}}{C_{11}C_{22} - C_{12}^2}$ [43], and for β-phase, d_{31} coefficient can be defined as $d_{31} = \frac{e_{31}}{C_{11} + C_{22}}$ [44]. The calculated C_{11}, C_{12}, C_{22}, e_{11}, e_{12}, d_{11}, and d_{12} coefficients for α-phase and γ-phase are summarized in Table S1 in the ESM and C_{11}, C_{12}, e_{31}, and d_{31} coefficients for β-phase are summarized in Table S2 in the ESM. All the e_{31} values of β-phase MX are less than 0.6×10^{-10} C/m, so we especially focus on the in-plane piezoelectricity in this work. The piezoelectric stress tensor e_{11} and corresponding piezoelectric strain tensor d_{11} for α-phase and γ-phase are shown in Fig. 5(a). Detail results are listed in Table S1 in the ESM. Density functional perturbation theory (DFPT) method is performed to double-check the reliability of the calculated results, and these two approaches show good agreement with each other as shown in Table S1 in the ESM. We find that all the d_{11} values of our studied 2D FE materials as listed in Table S1 in the ESM are obviously larger than bulk materials, including α-quartz and wurtzite (GaN and AlN) (estimated as 2.3, 3.1, and 5.1 pm/V) [45, 46], which are widely used in industry. Most in-plane relaxed d_{11} except for γ-AsP and γ-SbAs are larger than previously predicted transition metal dichalcogenides (estimated to be 2.12 ~ 13.5 pm/V) [44, 47, 48]. Particularly, α-SnTe has the largest e_{11} and d_{11} values, exceeding the α-SnSe that was predicted to possess superior in-plane piezoelectric properties [49].

To explore variation trends of the in-plane piezoelectric in α-phase and γ-phase MX, we plot the e_{11} of α-phase and γ-phase MX in Fig. 5(b). When fixing the M, the magnitude of e_{11} of MX consisting of Group IV and VI elements increases with the atomic number of X increasing, while those of MX consisting of both Group V elements show reverse trend. To analyze this phenomenon, we calculate the two parts e_{11}^{elc} and e_{11}^{ion} composed e_{11} for 2D materials as defined before [50–56]. As demonstrated in Table S3 in the ESM, e_{11}^{elc} is much less than e_{11}^{ion}, for most of our studied materials, the ion-part mainly contributes to the piezoelectric properties. The ionic contribution can be calculated according to Eq. (5)

$$e_{ij}^{\mathrm{ion}}(k) = \sum_k \frac{ea}{A} Z_{\mathrm{mi}}^{*}(k) \frac{du_{\mathrm{m}}(k)}{d\eta_j} \quad (5)$$

where e is the electron charge, A is the area of a unit cell, a is the lattice constant along polarization direction, $Z_{mi}^{*}(k)$ is the dynamical charge, u_m is the internal atomic coordinates, and η_j denotes the applied strain, respectively.

Here, for α-phase MX and γ-phase MX, the two factors mainly contributed to e_{11} are the dynamical charge of M atom (Z_{11}(M)) and the x-displacement of M atom with strain along x-direction ($du_1/d\eta_1$), which are summarized in Fig. 5(b) and Table S3 in the ESM. As demonstrated in previous literature [57], both electronegativity difference and the vertical distance between M atom and X atom which causes structural distortion, influence the magnitude of dynamical charge of FE materials. Our results show that the electronegativity difference between M and X atoms dominates in MX consisting of Group IV and VI elements as shown in Fig. 5(b). The lower electronegativity difference, the larger dynamical charge. While structural distortion also plays a

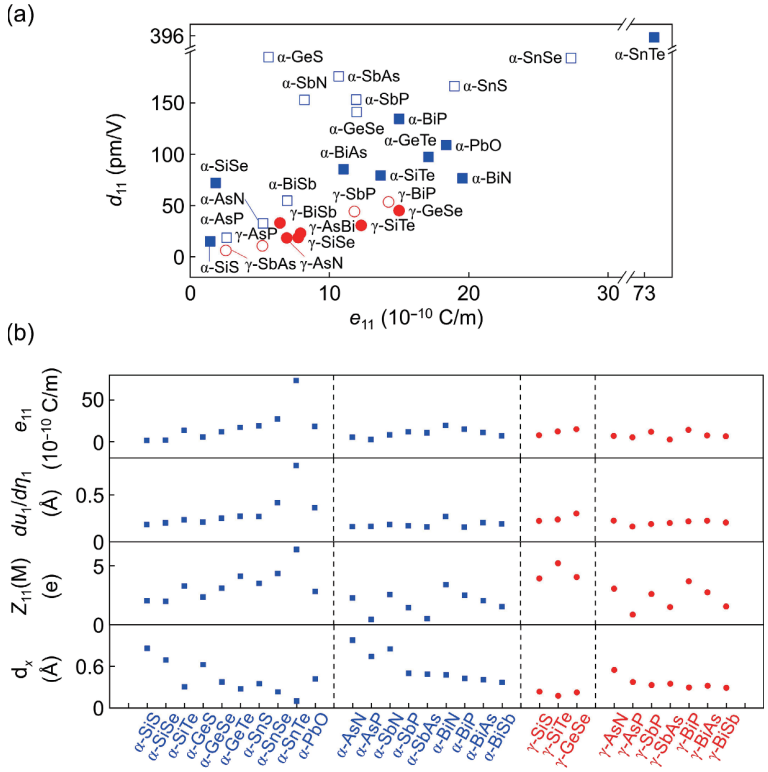

Figure 5 In-plane piezoelectric properties of α-phase and γ-phase MX. (a) Piezoelectric stress tensor (e_{11}) and corresponding piezoelectric strain tensor (d_{11}) of α-phase and γ-phase MX. The symbols in blue and red represent α-phase and γ-phase MX, respectively. The hollow symbols represent previously predicted compounds, while the solid symbols represent newly discovered MX in this work. (b) The e_{11}, the *x*-displacement of M atom with strain along *x*-direction ($d\mu_1/d\eta_1$), dynamical charge of M atom (Z_{11}(M)), and d_x as mentioned in Fig. 2(a) of α-phase (blue squares) and γ-phase (red dots) MX.

vital role in MX consisting of both Group V elements. The lower structural distortion, the lower dynamical charge.

3 Conclusions

In conclusion, by using high-throughput calculations we discover 39 new 2D FE MX compounds with 10 valance electrons from three phosphorus-analogue phases, including 15 in-plane and 24 out-of-plane ferroelectric materials. Both ferroelectricity and in-plane piezoelectricity are rationalized on the basis of dynamical charge transfer influenced by electronegativity and structural distortion. General trend that the larger the electronegativity difference between M and X becomes, the larger the ferroelectric polarization is observed. Larger electronegativity differences result in lower in-plane piezoelectric stress tensor for MX consisting of Group IV and VI elements and larger e_{11} for those consisting of Group V elements. Moreover, a giant TER effect of 1.26×10^4% far greater than the reported in-plane ferroelectric tunnel junction and a maximum d_{11} = 396 pm/V larger than α-SnSe have been achieved in α-Sb(Sn)P/α-SbP/α-Sb(Te)P FTJ and α-SnTe, respectively. Our findings largely expand the family of 2D FE MX materials and also explain general trends over broad compositional spaces, paving the way for the development of future memory and flexible nanoscale devices.

4 Methods

Density functional theory calculations are performed by using the Vienna *ab initio* simulation package [58–60] within the generalized gradient approximation of the Perdew–Burke–Ernzerhof (PBE) functional [61]. An energy cutoff of 600 eV is used for the plane-wave basis set and the *k* points sampling is Γ-centered 15 × 15 × 1. The vacuum length is larger than 15 Å along the *z*-axis. All the structures are relaxed until the energy converged to 10^{-7} eV and the interaction force on each atom is below 0.001 eV/Å. The phonon dispersion spectrum is calculated using the DFPT method as implemented in Phonopy code [62]. For the process of screening dynamical stability, we use 3 × 3 supercell with a 5 × 5 × 1 *k*-points. 5 ps *ab initio* molecular dynamical simulations (AIMD) were performed under canonical ensemble (NVT) [63, 64] at 300 K. The effect of SOC was achieved by a second variational procedure on a fully self-consistent basis. The formation enthalpies of other compounds made up of M element and X element except for the predicted MX compounds are all obtained from the Materials Project database by using the Materials Project REST API [65, 66]. The transport property calculations are performed by using the Nanodcal package [67], which is based on DFT plus non-equilibrium Green's function formalism (DFT + NEGF approach) [68]. The energy cutoff is setting as 100 Hartree. The *k*-point mesh for the self-consistent (SC) calculation is 300 × 300 × 300 and 3,000 × 3,000 × 3,000 for transmission calculations.

Acknowledgements

This work was supported by grants from the National Natural Science Foundation of China (Nos. 52272172, 61888102, and 52102193), the Major Program of National Natural Science Foundation of China (No. 92163206), and the Strategic Priority Research Program of the Chinese Academy of Sciences (No. XDB30000000), and the Fundamental Research Funds for the Central Universities. Computational resources were provided by the National Supercomputing Center in Tianjin.

Electronic Supplementary Material: Supplementary material (phonon spectrums of 39 new FE MX monolayers; band structures of FTJ electrode; spontaneous polarization and Bader charge of γ-phase; vertical distance between M atom and X atom which causes structural distortion of α-phase, β-phase, and γ-

phase; piezoelectric coefficients) is available in the online version of this article at https://doi.org/10.1007/s12274-022-5213-6.

References

[1] Li, B. C.; Li, S. F.; Wang, H.; Chen, L.; Liu, L.; Feng, X. W.; Li, Y. S.; Chen, J. S.; Gong, X.; Ang, K. W. An electronic synapse based on 2D ferroelectric $CuInP_2S_6$. *Adv. Electron. Mater.* **2020**, *6*, 2000760.

[2] Kwon, K. C.; Zhang, Y. S.; Wang, L.; Yu, W.; Wang, X. J.; Park, I. H.; Choi, H. S.; Ma, T.; Zhu, Z. Y.; Tian, B. B. et al. In-plane ferroelectric tin monosulfide and its application in a ferroelectric analog synaptic device. *ACS Nano* **2020**, *14*, 7628–7638.

[3] Liu, F. C.; You, L.; Seyler, K. L.; Li, X. B.; Yu, P.; Lin, J. H.; Wang, X. W.; Zhou, J. D.; Wang, H.; He, H. Y. et al. Room-temperature ferroelectricity in $CuInP_2S_6$ ultrathin flakes. *Nat. Commun.* **2016**, *7*, 12357.

[4] Cui, C. J.; Hu, W. J.; Yan, X. X.; Addiego, C.; Gao, W. P.; Wang, Y.; Wang, Z.; Li, L. Z.; Cheng, Y. C.; Li, P. et al. Intercorrelated in-plane and out-of-plane ferroelectricity in ultrathin two-dimensional layered semiconductor In_2Se_3. *Nano Lett.* **2018**, *18*, 1253–1258.

[5] Cui, C. J.; Xue, F.; Hu, W. J.; Li, L. J. Two-dimensional materials with piezoelectric and ferroelectric functionalities. *npj 2D Mater. Appl.* **2018**, *2*, 18.

[6] Brehm, J. A.; Neumayer, S. M.; Tao, L.; O'hara, A.; Chyasnavichus, M.; Susner, M. A.; Mcguire, M. A.; Kalinin, S. V.; Jesse, S.; Ganesh, P. et al. Tunable quadruple-well ferroelectric van der Waals crystals. *Nat. Mater.* **2020**, *19*, 43–48.

[7] Shen, X. W.; Tong, W. Y.; Gong, S. J.; Duan, C. G. Electrically tunable polarizer based on 2D orthorhombic ferrovalley materials. *2D Mater.* **2018**, *5*, 011001.

[8] Liu, S.; Kim, Y.; Tan, L. Z.; Rappe, A. M. Strain-induced ferroelectric topological insulator. *Nano Lett.* **2016**, *16*, 1663–1668.

[9] Jin, X.; Tao, L.; Zhang, Y. Y.; Pan, J. B.; Du, S. X. Intrinsically scale-free ferroelectricity in two-dimensional $M_2X_2Y_6$. *Nano Res.* **2022**, *15*, 3704–3710.

[10] Qi, L.; Ruan, S. C.; Zeng, Y. J. Review on recent developments in 2D ferroelectrics: Theories and applications. *Adv. Mater.* **2021**, *33*, 2005098.

[11] Barraza-Lopez, S.; Fregoso, B. M.; Villanova, J. W.; Parkin, S. S. P.; Chang, K. Colloquium: Physical properties of Group-IV monochalcogenide monolayers. *Rev. Mod. Phys.* **2021**, *93*, 011001.

[12] Bao, D. L.; O'Hara, A.; Du, S. X.; Pantelides, S. T. Tunable, ferroelectricity-inducing, spin-spiral magnetic ordering in monolayer FeOCl. *Nano Lett.* **2022**, *22*, 3598–3603.

[13] Xiao, J.; Zhu, H. Y.; Wang, Y.; Feng, W.; Hu, Y. X.; Dasgupta, A.; Han, Y. M.; Wang, Y.; Muller, D. A.; Martin, L. W. et al. Intrinsic two-dimensional ferroelectricity with dipole locking. *Phys. Rev. Lett.* **2018**, *120*, 227601.

[14] Yuan, S. G.; Luo, X.; Chan, H. L.; Xiao, C. C.; Dai, Y. W.; Xie, M. H.; Hao, J. H. Room-temperature ferroelectricity in $MoTe_2$ down to the atomic monolayer limit. *Nat. Commun.* **2019**, *10*, 1775.

[15] Chang, K.; Liu, J. W.; Lin, H. C.; Wang, N.; Zhao, K.; Zhang, A. M.; Jin, F.; Zhong, Y.; Hu, X. P.; Duan, W. H. et al. Discovery of robust in-plane ferroelectricity in atomic-thick SnTe. *Science* **2016**, *353*, 274–278.

[16] Higashitarumizu, N.; Kawamoto, H.; Lee, C. J.; Lin, B. H.; Chu, F. H.; Yonemori, I.; Nishimura, T.; Wakabayashi, K.; Chang, W. H.; Nagashio, K. Purely in-plane ferroelectricity in monolayer SnS at room temperature. *Nat. Commun.* **2020**, *11*, 2428.

[17] Chang, K.; Küster, F.; Miller, B. J.; Ji, J. R.; Zhang, J. L.; Sessi, P.; Barraza-Lopez, S.; Parkin, S. S. P. Microscopic manipulation of ferroelectric domains in SnSe monolayers at room temperature. *Nano Lett.* **2020**, *20*, 6590–6597.

[18] Walsh, A.; Payne, D. J.; Egdell, R. G.; Watson, G. W. Stereochemistry of post-transition metal oxides: Revision of the classical lone pair model. *Chem. Soc. Rev.* **2011**, *40*, 4455–4463.

[19] Laurita, G.; Seshadri, R. Chemistry, structure, and function of lone pairs in extended solids. *Acc. Chem. Res.* **2022**, *55*, 1004–1014.

[20] Wu, M. H.; Zeng, X. C. Intrinsic ferroelasticity and/or multiferroicity in two-dimensional phosphorene and phosphorene analogues. *Nano Lett.* **2016**, *16*, 3236–3241.

[21] Xu, T.; Zhang, J. T.; Zhu, Y. Q.; Wang, J.; Shimada, T.; Kitamura, T.; Zhang, T. Y. Two-dimensional polar metal of a PbTe monolayer by electrostatic doping. *Nanoscale Horiz.* **2020**, *5*, 1400–1406.

[22] Shen, S. Y.; Liu, C.; Ma, Y. D.; Huang, B. B.; Dai, Y. Robust two-dimensional ferroelectricity in single-layer γ-SbP and γ-SbAs. *Nanoscale* **2019**, *11*, 11864–11871.

[23] Guan, S.; Liu, C.; Lu, Y. H.; Yao, Y. G.; Yang, S. A. Tunable ferroelectricity and anisotropic electric transport in monolayer β-GeSe. *Phys. Rev. B* **2018**, *97*, 144104.

[24] Wang, H.; Qian, X. F. Two-dimensional multiferroics in monolayer Group IV monochalcogenides. *2D Mater.* **2017**, *4*, 015042.

[25] Wang, H.; Qian, X. F. Giant optical second harmonic generation in two-dimensional multiferroics. *Nano Lett.* **2017**, *17*, 5027–5034.

[26] Ding, W. J.; Zeng, J.; Qin, W.; Cui, P.; Zhang, Z. Y. Exploring high transition temperature superconductivity in a freestanding or $SrTiO_3$-supported CoSb monolayer. *Phys. Rev. Lett.* **2020**, *124*, 027002.

[27] Yang, J. H.; Zhang, Y. Y.; Yin, W. J.; Gong, X. G.; Yakobson, B. I.; Wei, S. H. Two-dimensional SiS layers with promising electronic and optoelectronic properties: Theoretical prediction. *Nano Lett.* **2016**, *16*, 1110–1117.

[28] Barber, C. B.; Dobkin, D. P.; Huhdanpaa, H. The quickhull algorithm for convex hulls. *ACM Trans. Math. Softw.* **1996**, *22*, 469–483.

[29] Song, Y.; Pan, J. B.; Zhang, Y. F.; Yang, H. T.; Du, S. X. Monolayer iridium sulfide halides with high mobility transport anisotropy and highly efficient light harvesting. *J. Phys. Chem. Lett.* **2021**, *12*, 6007–6013.

[30] Haastrup, S.; Strange, M.; Pandey, M.; Deilmann, T.; Schmidt, P. S.; Hinsche, N. F.; Gjerding, M. N.; Torelli, D.; Larsen, P. M.; Riis-Jensen, A. C. et al. The computational 2D materials database: High-throughput modeling and discovery of atomically thin crystals. *2D Mater.* **2018**, *5*, 042002.

[31] Gjerding, M. N.; Taghizadeh, A.; Rasmussen, A.; Ali, S.; Bertoldo, F.; Deilmann, T.; Knøsgaard, N. R.; Kruse, M.; Larsen, A. H.; Manti, S. et al. Recent progress of the computational 2D materials database (C2DB). *2D Mater.* **2021**, *8*, 044002.

[32] Henkelman, G.; Uberuaga, B. P.; Jónsson, H. A climbing image nudged elastic band method for finding saddle points and minimum energy paths. *J. Chem. Phys.* **2000**, *113*, 9901–9904.

[33] Henkelman, G.; Jónsson, H. Improved tangent estimate in the nudged elastic band method for finding minimum energy paths and saddle points. *J. Chem. Phys.* **2000**, *113*, 9978–9985.

[34] Sheppard, D.; Xiao, P. H.; Chemelewski, W.; Johnson, D. D.; Henkelman, G. A generalized solid-state nudged elastic band method. *J. Chem. Phys.* **2012**, *136*, 074103.

[35] Spaldin, N. A. A beginner's guide to the modern theory of polarization. *J. Solid State Chem.* **2012**, *195*, 2–10.

[36] Ghosez, P.; Michenaud, J. P.; Gonze, X. Dynamical atomic charges: The case of ABO_3 compounds. *Phys. Rev. B* **1998**, *58*, 6224–6240.

[37] King-Smith, R. D.; Vanderbilt, D. Theory of polarization of crystalline solids. *Phys. Rev. B* **1993**, *47*, 1651–1654.

[38] Resta, R. Macroscopic polarization in crystalline dielectrics: The geometric phase approach. *Rev. Mod. Phys.* **1994**, *66*, 899–915.

[39] Kamal, C.; Chakrabarti, A.; Ezawa, M. Direct band gaps in Group IV-VI monolayer materials: Binary counterparts of phosphorene. *Phys. Rev. B* **2016**, *93*, 125428.

[40] Velev, J. P.; Duan, C. G.; Burton, J. D.; Smogunov, A.; Niranjan, M. K.; Tosatti, E.; Jaswal, S. S.; Tsymbal, E. Y. Magnetic tunnel junctions with ferroelectric barriers: Prediction of four resistance states from first principles. *Nano Lett.* **2009**, *9*, 427–432.

[41] Shen, X. W.; Fang, Y. W.; Tian, B. B.; Duan, C. G. Two-dimensional ferroelectric tunnel junction: The case of monolayer In:SnSe/SnSe/Sb:SnSe homostructure. *ACS Appl. Electron. Mater.* **2019**, *1*, 1133–1140.

[42] Kang, L. L.; Jiang, P.; Cao, N.; Hao, H.; Zheng, X. H.; Zhang, L.; Zeng, Z. Realizing giant tunneling electroresistance in two-dimensional graphene/BiP ferroelectric tunnel junction. *Nanoscale* **2019**, *11*, 16837–16843.

[43] Yin, H. B.; Gao, J. W.; Zheng, G. P.; Wang, Y. X.; Ma, Y. C. Giant piezoelectric effects in monolayer Group-V binary compounds with

honeycomb phases: A first-principles prediction. *J. Phys. Chem. C* **2017**, *121*, 25576–25584.
[44] Blonsky, M. N.; Zhuang, H. L.; Singh, A. K.; Hennig, R. G. *Ab initio* prediction of piezoelectricity in two-dimensional materials. *ACS Nano* **2015**, *9*, 9885–9891.
[45] Bechmann, R. Elastic and piezoelectric constants of alpha-quartz. *Phys. Rev.* **1958**, *110*, 1060–1061.
[46] Bernardini, F.; Fiorentini, V.; Vanderbilt, D. Polarization-based calculation of the dielectric tensor of polar crystals. *Phys. Rev. Lett.* **1997**, *79*, 3958–3961.
[47] Coleman, J. N.; Lotya, M.; O'neill, A.; Bergin, S. D.; King, P. J.; Khan, U.; Young, K.; Gaucher, A.; De, S.; Smith, R. J. et al. Two-dimensional nanosheets produced by liquid exfoliation of layered materials. *Science* **2011**, *331*, 568–571.
[48] Zhu, H. Y.; Wang, Y.; Xiao, J.; Liu, M.; Xiong, S. M.; Wong, Z. J.; Ye, Z. L.; Ye, Y.; Yin, X. B.; Zhang, X. Observation of piezoelectricity in free-standing monolayer MoS_2. *Nat. Nanotechnol.* **2015**, *10*, 151–155.
[49] Fei, R. X.; Li, W. B.; Li, J.; Yang, L. Giant piezoelectricity of monolayer Group IV monochalcogenides: SnSe, SnS, GeSe, and GeS. *Appl. Phys. Lett.* **2015**, *107*, 173104.
[50] Dal Corso, A.; Posternak, M.; Resta, R.; Baldereschi, A. *Ab initio* study of piezoelectricity and spontaneous polarization in ZnO. *Phys. Rev. B* **1994**, *50*, 10715–10721.
[51] Bernardini, F.; Fiorentini, V.; Vanderbilt, D. Spontaneous polarization and piezoelectric constants of III-V nitrides. *Phys. Rev. B* **1997**, *56*, R10024–R10027.
[52] Sághi-Szabó, G.; Cohen, R. E.; Krakauer, H. First-principles study of piezoelectricity in $PbTiO_3$. *Phys. Rev. Lett.* **1998**, *80*, 4321–4324.
[53] Sághi-Szabó, G.; Cohen, R. E.; Krakauer, H. First-principles study of piezoelectricity in tetragonal $PbTiO_3$ and $PbZr_{1/2}Ti_{1/2}O_3$. *Phys. Rev. B* **1999**, *59*, 12771–12776.
[54] Bellaiche, L.; Vanderbilt, D. Virtual crystal approximation revisited: Application to dielectric and piezoelectric properties of perovskites. *Phys. Rev. B* **2000**, *61*, 7877–7882.
[55] Qi, Y. B.; Rappe, A. M. Widespread negative longitudinal piezoelectric responses in ferroelectric crystals with layered structures. *Phys. Rev. Lett.* **2021**, *126*, 217601.
[56] Noor-A-Alam, M.; Nolan, M. Negative piezoelectric coefficient in ferromagnetic 1H-$LaBr_2$ monolayer. *ACS Appl. Electron. Mater.* **2022**, *4*, 850–855.
[57] Wu, Y. Z.; Abdelwahab, I.; Kwon, K. C.; Verzhbitskiy, I.; Wang, L.; Liew, W. H.; Yao, K.; Eda, G.; Loh, K. P.; Shen, L. et al. Data-driven discovery of high performance layered van der Waals piezoelectric $NbOI_2$. *Nat. Commun.* **2022**, *13*, 1884.
[58] Kresse, G.; Hafner, J. *Ab initio* molecular dynamics for open-shell transition metals. *Phys. Rev. B* **1993**, *48*, 13115–13118.
[59] Kresse, G.; Hafner, J. *Ab initio* molecular dynamics for liquid metals. *Phys. Rev. B* **1993**, *47*, 558–561.
[60] Kresse, G.; Furthmüller, J. Efficiency of *ab-initio* total energy calculations for metals and semiconductors using a plane-wave basis set. *Comput. Mater. Sci.* **1996**, *6*, 15–50.
[61] Perdew, J. P.; Burke, K.; Ernzerhof, M. Generalized gradient approximation made simple. *Phys. Rev. Lett.* **1996**, *77*, 3865–3868.
[62] Togo, A.; Tanaka, I. First principles phonon calculations in materials science. *Scr. Mater.* **2015**, *108*, 1–5.
[63] Nosé, S. A molecular dynamics method for simulations in the canonical ensemble. *Mol. Phys.* **1984**, *52*, 255–268.
[64] Nosé, S. A unified formulation of the constant temperature molecular dynamics methods. *J. Chem. Phys.* **1984**, *81*, 511–519.
[65] Ong, S. P.; Cholia, S.; Jain, A.; Brafman, M.; Gunter, D.; Ceder, G.; Persson, K. A. The materials application programming interface (API): A simple, flexible and efficient API for materials data based on REpresentational State Transfer (REST) principles. *Comput. Mater. Sci.* **2015**, *97*, 209–215.
[66] Paier, J.; Hirschl, R.; Marsman, M.; Kresse, G. The Perdew–Burke–Ernzerhof exchange-correlation functional applied to the G2-1 test set using a plane-wave basis set. *J. Chem. Phys.* **2005**, *122*, 234102.
[67] Maassen, J.; Harb, M.; Michaud-Rioux, V.; Zhu, Y.; Guo, H. Quantum transport modeling from first principles. *Proc. IEEE* **2013**, *101*, 518–530.
[68] Taylor, J.; Guo, H.; Wang, J. *Ab initio* modeling of quantum transport properties of molecular electronic devices. *Phys. Rev. B* **2001**, *63*, 245407.
[69] Wan, W. H.; Liu, C.; Xiao, W. D.; Yao, Y. G. Promising ferroelectricity in 2D Group IV tellurides: A first-principles study. *Appl. Phys. Lett.* **2017**, *111*, 132904.
[70] Jia, Y. Z.; Luo, F. X.; Hao, X. M.; Meng, Q. L.; Dou, W. Z.; Zhang, L.; Wu, J. G.; Zhai, S. W.; Zhou, M. Intrinsic valley polarization and high-temperature ferroelectricity in two-dimensional orthorhombic lead oxide. *ACS Appl. Mater. Interfaces* **2021**, *13*, 6480–6488.
[71] Liu, C.; Wan, W. H.; Ma, J.; Guo, W.; Yao, Y. G. Robust ferroelectricity in two-dimensional SbN and BiP. *Nanoscale* **2018**, *10*, 7984–7990.
[72] Chen, P.; Zhang, X. J.; Liu, B. G. Mechanically-controllable strong 2D ferroelectricity and optical properties of semiconducting BiN monolayer. *ACS Appl. Nano Mater.* **2019**, *2*, 58–63.
[73] Liu, C.; Guan, S.; Yin, H. B.; Wan, W. H.; Wang, Y. X.; Zhang, Y. γ-GeSe: A two-dimensional ferroelectric material with doping-induced ferromagnetism. *Appl. Phys. Lett.* **2019**, *115*, 252904.